

Large-Scale Integration of a Zinc Metasilicate Interface Layer Guiding Well-Regulated Zn Deposition

Ruiting Guo, Xiong Liu,* Fanjie Xia, Yalong Jiang, Huazhang Zhang, Meng Huang, Chaojiang Niu, Jinsong Wu, Yan Zhao, Xuanpeng Wang, Chunhua Han,* and Liqiang Mai*

Uneven distribution of electric fields at the electrolyte–anode interface and associated Zn dendrite growth is one of the most critical barriers that limit the life span of aqueous zinc-ion batteries. Herein, new-type Zn–A–O (A = Si, Ti) interface layers with thin and uniform thickness, porosity, and hydrophilicity properties are developed to realize homogeneous and smooth Zn plating. For ZnSiO₃ nanosheet arrays on Zn foil (Zn@ZSO), their formation follows an “etching–nucleation–growth” mechanism that is confirmed by a well-designed Zn-island-based identical-location microscopy method, the geometric area of which is up to 1000 cm² in one-pot synthesis based on a low-temperature wet-chemical method. Guided by the structural advantages of the ZSO layer, the Zn²⁺ flux gets equalized. Besides ultralow polarization, the life spans of symmetric cells and full cells coupled with a high-mass-loading K_{0.27}MnO₂·0.54H₂O (8 mg cm⁻²) cathode, are increased by 3–7 times with the Zn@ZSO anode. Moreover, the large-scale preparation of Zn@ZSO foil contributes to a 0.5 Ah multilayer pouch cell with high performance, further confirming its prospects for practical application.

1. Introduction

Due to the advantages of high safety and environmental friendliness, aqueous batteries (ABs) are regarded as one of the most competitive candidates for large-scale energy storage, which have become a research hotspot in recent years.^[1,2] In a series of metal-ion ABs, including Li-, Na-, K-, Mg-, Ca-, Al-, and Zn-ion batteries, due to the appropriate redox potential of Zn²⁺/Zn couple (−0.76 V vs standard hydrogen electrode), Zn metal is relatively stable in water and can be directly used as an anode, which also exhibits a high volumetric energy density


(5855 mAh cm⁻³) and better plating/stripping reversibility than Mg, Ca, and Al.^[3] In addition, as an earth-abundant metal, the price of Zn is only ≈4% of Li.^[4] Therefore, aqueous zinc-ion batteries (AZIBs) have ushered in an unprecedented development in the past few years. Considerable efforts have been made to further improve the reversibility of Zn plating/stripping.^[5,6] At the same time, it should be noted that the dendrite growth caused by uneven Zn plating can not only reduce the reversibility, but also directly cause a short circuit after penetrating the separator, seriously limiting the life span of AZIBs.^[7,8]

Regulating Zn plating behavior at electrolyte–anode interface to realize smooth Zn deposition is necessary to stabilize Zn anode.^[9,10] One of the main methods is electrolyte regulation,^[11] including designing unique electrolyte systems,^[12–14] using electrolyte additives,^[15,16] developing gel

electrolytes,^[17] etc. Another key strategy is Zn anode surface modification, namely constructing artificial interface layer on Zn foil. Recently, various materials including organics (polyamide,^[18] polyacrylonitrile,^[19] poly(vinyl butyral),^[20] etc.) and inorganics (TiO₂,^[21] CaCO₃,^[22] ZrO₂,^[23] Al₂O₃,^[24] etc.) have been constructed as protective interface layers by doctor blading, spin coating, or atomic layer deposition (ALD) methods. However, they face some practical limitations, including difficulty in controlling consistency of layer composition/structure and thickness, or inability to accommodate easy mass production. For example, additional binders are required for doctor-blading

R. Guo, F. Xia, Y. Jiang, M. Huang, J. Wu, Y. Zhao, C. Han, L. Mai
State Key Laboratory of Advanced Technology for Materials Synthesis
and Processing
Wuhan University of Technology
Wuhan 430070, China
E-mail: hch5927@whut.edu.cn; mlq518@whut.edu.cn

X. Liu, C. Niu
School of Materials Science and Engineering
Zhengzhou University
Zhengzhou 450001, China
E-mail: liuxiong@zzu.edu.cn

 The ORCID identification number(s) for the author(s) of this article can be found under <https://doi.org/10.1002/adma.202202188>.

H. Zhang, X. Wang
Department of Physical Science & Technology, School of Science
Wuhan University of Technology
Wuhan 430070, China

X. Wang, L. Mai
Foshan Xianhu Laboratory of the Advanced Energy Science and
Technology Guangdong Laboratory
Xianhu hydrogen Valley
Foshan 528200, China

L. Mai
Hubei Longzhong Laboratory
Xiangyang, Hubei 441000, China

DOI: 10.1002/adma.202202188

method, which may result in uneven distribution of layer components and obstruct the mass transport. Meanwhile, the coating thickness is unmanageable and often up to tens of micrometers,^[21,25,26] causing increased weight of anode and finally reducing the energy density. Thick coating layer with poor electronic conductivity can lead to large interfacial resistance,^[27] and may also affect the flexibility and foldability of Zn foil. ALD method can be used to prepare ultrathin coatings with controllable thickness at nanometer level,^[24] but the types of coatings are limited and so far it is still difficult to achieve low-cost and large-scale production.^[28] In principle, Zn-based compounds can form in situ on the Zn surface through the reaction between raw materials and Zn foil, and build tight connections with Zn surface. Recently, ZnF₂,^[29,30] ZnO,^[31] ZnS,^[32] and Zn₃(PO₄)₂·4H₂O^[33] have been studied as interface layers, showing the potential of Zn-based compounds on Zn anode protection. Nevertheless, it is still a challenge to construct highly uniform, thin, and affordable interface layer via a scalable method.

In this work, a thin interface layer composed of ZnSiO₃ (ZSO) nanosheet arrays has been in situ integrated on Zn foil surface by a facile wet-chemistry method. During reacting process, Zn²⁺ dissolves out due to the etching of hot alkaline solution, and nucleates with metasilicate ions when reaching a certain concentration, growing into tightly arranged ultrathin nanosheet array, namely, “etching–nucleation–growth” process. This in situ integration strategy ensures the uniformity of the layer and the tightness of its connection with the Zn foil. By the protection of the dense and fully covered ZSO layer, the side reaction to the formation of Zn₄SO₄(OH)₆·xH₂O gets mitigated. In addition, the evenly distributed micro-/mesopores on the ZSO nanosheets and the hydrophilic of the layer promote the charge/mass transfer processes, thus reducing the nucleation barrier and polarization. Moreover, Zn²⁺ flux is equalized by the uniform nanosheet array structure, increasing more active nucleation sites and reducing local current density, finally eliminating “tip effect.” As a result, the operating life span of symmetric cell and high-areal-capacity full cell both get extended several times.

2. Results and Discussion

2.1. Structural Features of the ZSO Layer

A low-temperature wet-chemistry method was used to prepare Zn@ZSO composite foil, and the details are shown in the Experimental Section of the Supporting Information. The formation of the layer follows an “etching–nucleation–growth” process as illustrated in **Figure 1a**, ending uniform and in situ integration of Zn–Si–O layer on Zn foil. In small-scale preparation, the bare Zn foil completely turned from silver to celadon after reaction (**Figure S1a**, Supporting Information), indicating the uniform growth and full coverage of the interface layer. Large-area Zn@ZSO sample of 1000 cm² was obtained by upscaling the amounts of raw materials and the size of reactor (**Figure 1b** and **Figure S1b** (Supporting Information)). The uniformity of the layer and large-scale production of the composite Zn foil are the key to realize multilayer high-capacity pouch cell and promote its application. According to

the low-magnification scanning electron microscopy (SEM) images, the ZSO layer is confirmed to be smooth and compact (**Figure S2a,b**, Supporting Information). In detail, it is composed of tightly packed nanosheet arrays and the thickness of a single nanosheet is ≈15 nm (**Figure 1c**). The existing cracks between nanosheets are conductive to the infiltration and transport of electrolyte. Notably, the morphologies at each position (including edge and center) in the large-area sample are consistent (**Figure S2c,d**, Supporting Information), indicating that the quality in mass production can be guaranteed. Moreover, after ultrasound in ethanol at 40 kHz for 5 h, the layer is still tightly connected to Zn foil and its morphology maintains well (**Figure S2e,f**, Supporting Information), confirming its strong combination with Zn surface.

The ZSO layer is too thin to obtain any structural information from X-ray diffraction pattern (**Figure S3**, Supporting Information), therefore, a thin section was prepared from bulk Zn@ZSO foil by a standard focused-ion beam (FIB) lift-out procedure (**Figure 1d**), to identify the phase structure of the layer. The region in the yellow dotted box was further observed by atomic-resolution high-angle annular dark-field scanning transmission electron microscopy (HAADF-STEM). As shown in **Figure 1e**, the ZSO layer adheres closely to the Zn surface, and the vertical thickness of the layer is very uniform that is determined as ≈300 nm. Zn, Si, and O elements are uniformly distributed in the layer region (**Figure 1f**), and the average Si/Zn atomic ratio in six regions is ≈1.09 (**Table S1**, Supporting Information). Furthermore, the diffraction rings in the selected area electron diffraction (SAED) pattern can be well-indexed as the (131), (631), and (023) crystal planes of ZnSiO₃ (JCPDS No. 70-0852) (**Figure S4a**, Supporting Information). The lattice fringes of 0.259, 0.287, 0.274, and 0.164 nm in the high-resolution transmission electron microscopy (HRTEM) images (**Figure 1g** and **Figure S4b** (Supporting Information)), can also be well-assigned to the (131), (610), (421), and (023) crystal planes of ZnSiO₃, respectively. These above results prove that the phase of the layer is ZnSiO₃. In addition, although the ultrathin nanosheets are densely arranged, they are rich in evenly distributed pore structures (**Figure 1h**), which can act as ion migration tunnels that will suppress inhomogeneous ion diffusion driven by the uneven electric field.^[8]

2.2. Integration Mechanism of the ZSO Functional Units

The ZSO layer has been confirmed to possess multiple characteristics, including thin thickness, uniformity, porosity, and tightness. To investigate the integration mechanism of such functional units on the Zn foil, a Zn-island-based identical-location SEM (IL-SEM) characterization was designed and operated for the first time to directly visualize the microstructure and component evolution during synthesis. First, Zn island loaded on the titanium foil (denoted as Ti@Zn) was prepared by electrodeposition method in 2 M ZnSO₄ solution (**Figure S5a**, Supporting Information). There are many monodisperse Zn islands with different shapes on the Ti surface (**Figure S5b**, Supporting Information), so any changes of one Zn island at different reaction stages can be observed by marking its location and surroundings at both macro- and

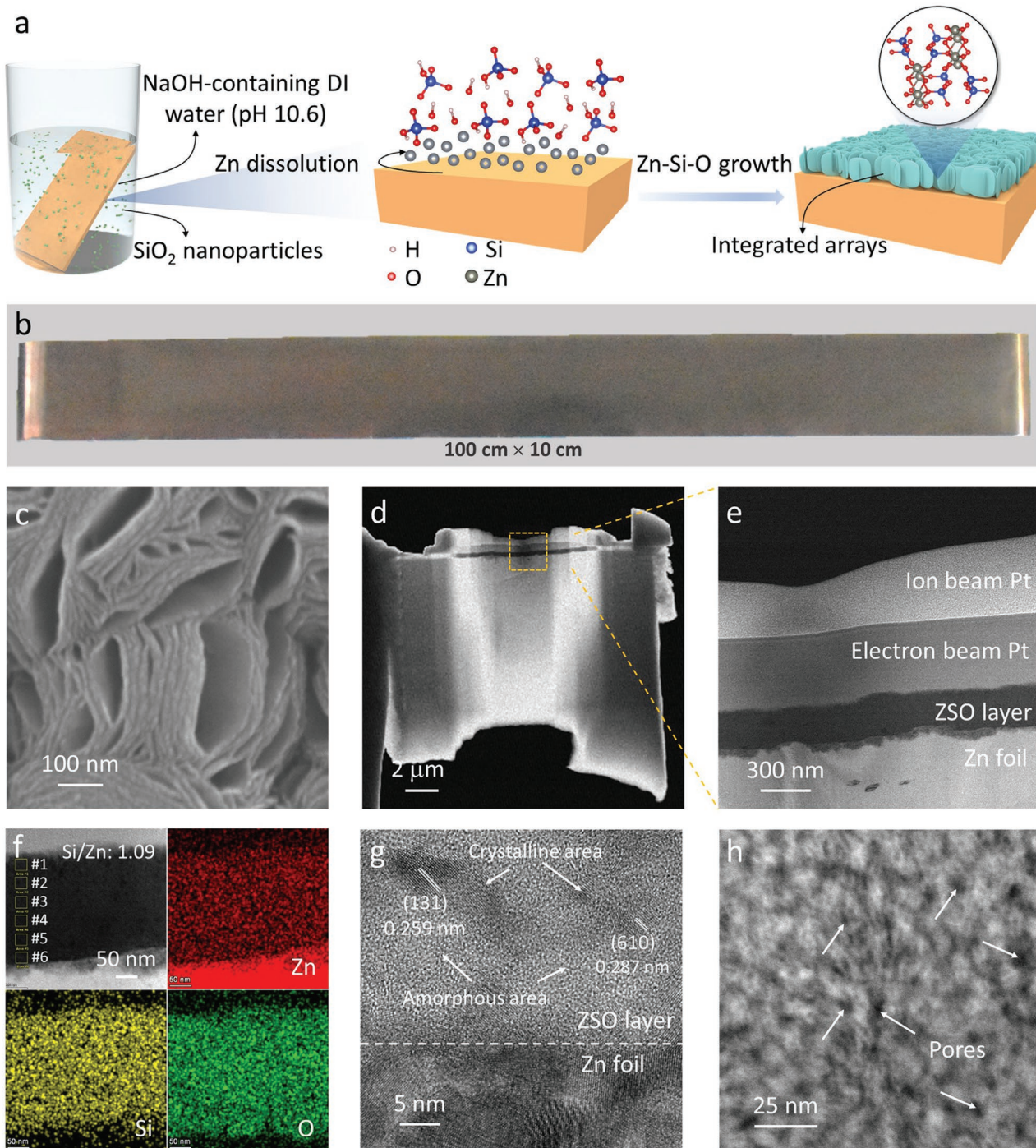
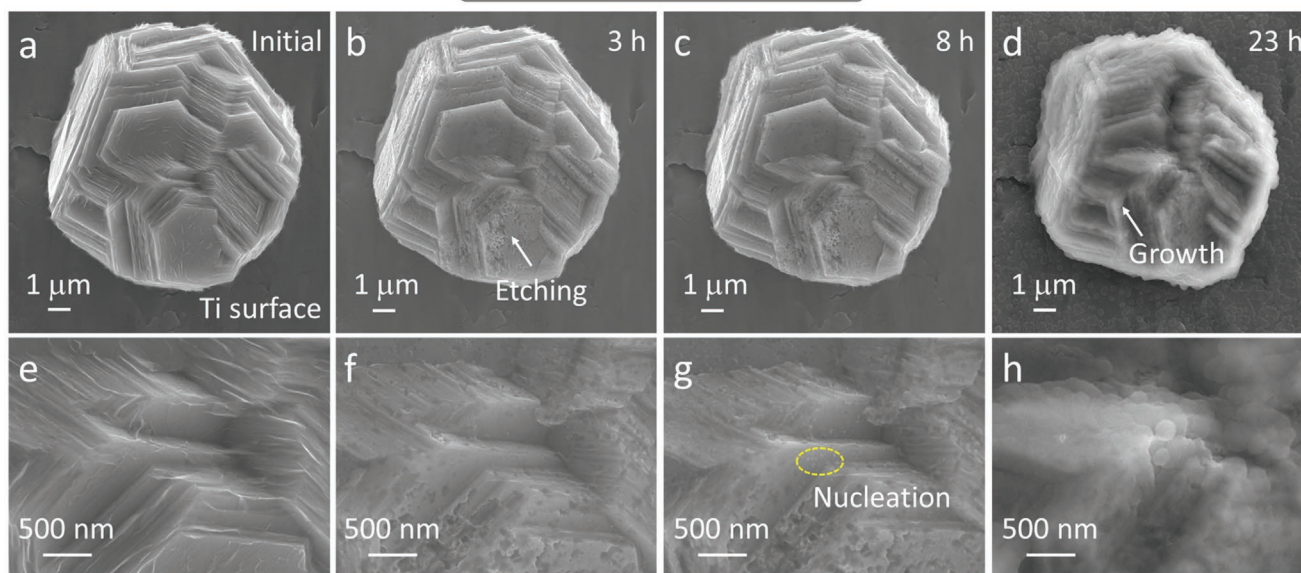


Figure 1. a) Schematic illustration of the procedure for fabricating the Zn@ZSO composite foil. b) Digital photo of the prepared large-area Zn@ZSO foil (100 cm × 10 cm). c) SEM image of the ZSO layer. d) FIB-STEM image of the prepared Zn@ZSO thin section. e) Cross-sectional HAADF-STEM image of Zn@ZSO thin section. f) HAADF-STEM image of ZSO layer and the corresponding elemental mappings, #1–6 are the selected areas for elemental content analysis. g) Cross-sectional HRTEM image of Zn–ZSO interface. h) HAADF-STEM image of ZSO layer.

microlevels (see details in Figure S6 in the Supporting Information). The pristine Zn island is composed of numerous stacked hexagonal sheets (Figure 2a,e). The flakes disappear and some holes appear on its surface after 3 h of reaction (Figure 2b,f and Figure S7a (Supporting Information)), indicating that the surface of Zn dissolves out due to the etching of hot alkaline

solution. After reacting for 8 h, the appeared tiny particles are supposed to be the seed crystal for the subsequent growth of Zn–Si–O layer (Figure 2c,g and Figure S7b (Supporting Information)). Zn island has been completely covered with compact particles after reacting for 23 h (Figure 2d,h). According to the corresponding elemental mapping results, the Si element is

IL-SEM characterization



Ex situ characterization

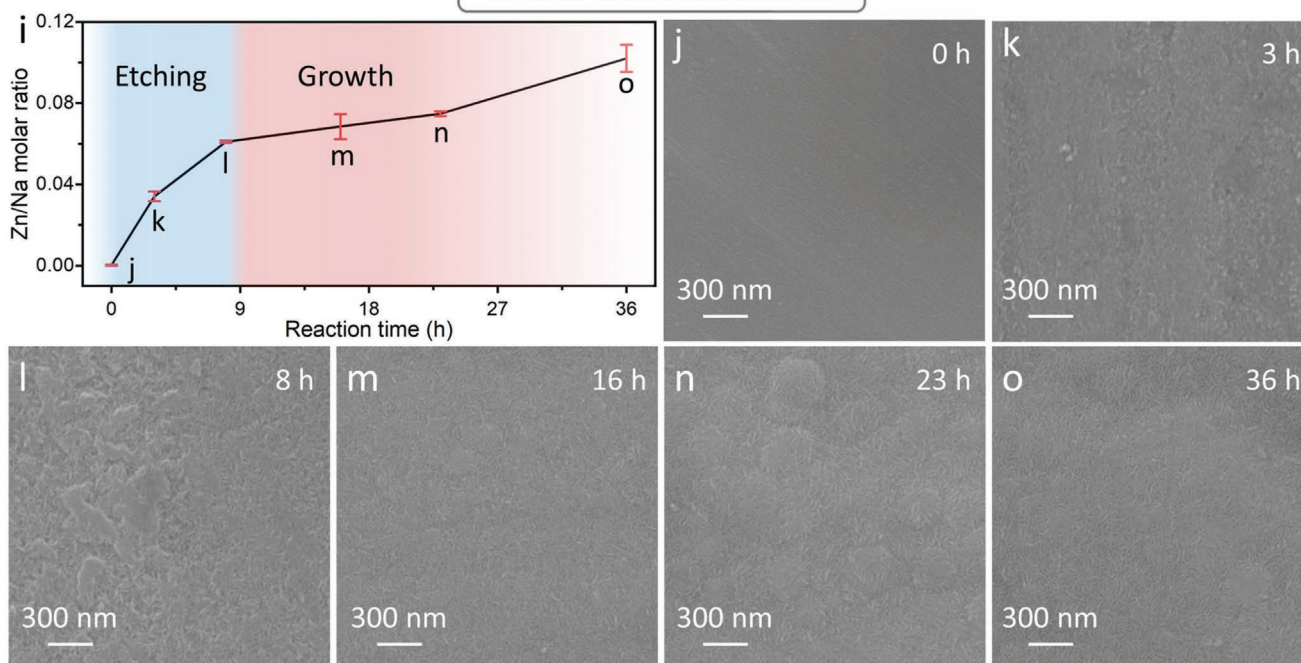


Figure 2. a–h) IL-SEM images of Ti@Zn initially (a,e), and after reacting for 3 h (b,f), 8 h (c,g), and 23 h (d,h), respectively. i) Zn/Na molar ratio values with error bars in the solution at different reaction stages. j–o) SEM images of Zn foil surface initially, and after reacting for 3, 8, 16, 23, and 36 h, respectively.

present and uniformly distributed on the Zn island in the 23 h sample (Figure S8, Supporting Information), and the particles are confirmed to be assembled by nanosheets (Figure S9a, Supporting Information). Therefore, the formation of ZSO is supposed to undergo an “etching–nucleation–growth” process. Because the initial pH value of the reaction solution is 10.6, the main existence form of SiO₂ raw material is HSiO₃[−].^[34] Hence, the formation of ZnSiO₃ layer is supposed to base on the

reaction: $\text{Zn}^{2+} + \text{HSiO}_3^- + \text{OH}^- \rightarrow \text{ZnSiO}_3 + \text{H}_2\text{O}$. In addition, the initial surface area of the Ti substrate away from the Zn island is bare, but monodisperse clusters of nanosheets appear in the 23 h sample (Figure S9b, Supporting Information), and such nanosheets further spread across the whole surface after reacting for 29 h (Figure S9c, Supporting Information). This phenomenon indicates that the integration of ZSO units and formation of ZSO layer are closely related to the concentration

of Zn^{2+} . When the concentration of Zn^{2+} in the solution reaches a certain value, Zn^{2+} and metasilicate ions will undergo codeposition via heterogeneous nucleation and growth, which will be further explained hereinafter.

To further elucidate the integration mechanism, the evolution of the elemental content in the solution and the surface structure of Zn foil at different reaction stages were studied by ex situ characterization. Zn and Na elemental contents in the solutions at different reaction stages were determined by inductively coupled plasma atomic emission spectrometry (ICP-AES) measurement. Since the content of Na in each solution is fixed, the measured Zn/Na molar ratio can reflect the changes of Zn content during reaction (Figure 2i). SEM images of the corresponding samples are also shown in Figure 2j–o. Initially, the surface of Zn foil is smooth before reaction. After reacting for 3 h, the Zn/Na molar ratio increases significantly from the initial 0.025% to 3.2%, and the Zn surface is observed with numerous holes, proving the dissolution of Zn. After 8 h, the Zn surface has been covered with growing ZSO species. As the reaction continues, the increase of Zn/Na ratios slows down due to the consumption of Zn^{2+} , and the ZSO layer on Zn surface becomes denser (16 and 23 h samples). Finally, as the reaction ends, the Zn content in the solution increases more.

The above IL-SEM and ex situ characterization results both support the proposed “etching–nucleation–growth” mechanism, compared with the latter, the characteristic of the former is that it observes a fixed place in one 3D Zn island. The reaction needs to be terminated and the sample needs to be washed before each SEM shooting, so the etching dissolution and growth process lag behind the continuous reaction. Therefore, time ranges for etching, nucleation, and growth processes can be better confirmed by ex situ ICP and SEM, while the changes on the material’s surface can be captured more clearly and accurately by IL-SEM. In general, the “etching–nucleation–growth” mechanism ensures the uniform formation of the layer. Even using SiO_2 nanoparticles with a diameter of 50 nm as raw material, the obtained ZSO layer is still consistent with that of 15 nm (Figure S10a, Supporting Information). As far as we know, it is the first time that such ZSO layer with unique structure is employed as the interface layer, so the exploration and demonstration of its formation mechanism is of reference value to the construction of other congeneric interface layers. For example, uniform and thin Zn–Ti–O interface layer on Zn foil can be obtained when SiO_2 is replaced by commercial TiO_2 , which also displays pretty nanosheet array structure (Figure S10b–d, Supporting Information).

2.3. Zn Plating/Stripping Performance of Zn@ZSO Electrode

The Zn surface tends to be corroded in mildly acidic electrolyte, e.g., 2 M ZnSO_4 with pH of 4.1. The released hydrogen will cause pressure inside the cell, and bulge of the cell when pressure continuously accumulates.^[29] Besides, the local rise in pH leads to the formation of $\text{Zn}_4\text{SO}_4(\text{OH})_6 \cdot x\text{H}_2\text{O}$ by-product,^[32] which will increase the interfacial impedance and cause uneven Zn plating. Therefore, reducing or even isolating the corrosion of Zn surface should be a basic function of the interface layer. Here, the related property of the ZSO layer was evaluated first by IL-SEM characterizations. After soaking in 2 M

ZnSO_4 aqueous solution for 3 h, Zn island has been completely covered with flake $\text{Zn}_4\text{SO}_4(\text{OH})_6 \cdot x\text{H}_2\text{O}$ (Figure S11a,b, Supporting Information). Actually, the surface of Zn island has changed after 10 min of immersion (Figure S11c,d, Supporting Information), indicating that the side reaction between Zn and electrolyte happens spontaneously and rapidly. While with the protection of the ZSO layer, the Zn@ZSO structure keeps intact after soaking for 3 h (Figure S11e,f, Supporting Information). It suggests the side reaction has been effectively retarded, and confirms the favorable chemical stability of the layer in electrolyte.

Next, symmetric cells were assembled to preliminarily assess the long-term cycling stability of bare Zn and Zn@ZSO electrodes. As shown in Figure 3a,b and Figure S12 (Supporting Information), with an areal capacity of 1 mAh cm^{-2} , the Zn@ZSO//Zn@ZSO symmetric cells operate steadily for 800 cycles (1600 h) and 3800 cycles (1520 h) at 1 and 5 mA cm^{-2} , about 75 and 4.5 times of Zn//Zn symmetric cells, respectively. The flatter voltage curves of Zn@ZSO//Zn@ZSO symmetric cells are thought to be derived from the uniform Zn plating/stripping driven by the fast kinetic of interfacial reaction and ion diffusion.^[35] Besides, the Zn@ZSO displays a much smaller voltage hysteresis of 21 mV than that of pure Zn (48 mV) at 1 mA cm^{-2} , and also has a very small voltage hysteresis of 62 mV even at high current density of 5 mA cm^{-2} , indicating the minor polarization in Zn@ZSO//Zn@ZSO symmetric cell. In the rate performance test, when the current densities increase from 0.5 to 5 mA cm^{-2} , the voltage hysteresis values of Zn@ZSO//Zn@ZSO symmetric cell are less than $\approx 1/2$ of that in the Zn//Zn symmetric cell (Figure S13, Supporting Information), and show lower magnitude of increase when the current density increases in a gradient, indicating its better rate performance. In addition, when returning to 0.5 mA cm^{-2} , a short circuit in Zn//Zn symmetric cell happened at the ninth cycle, showing the severe dendrite growth issue. When compared with the previously reported representative interface layers including Zn-based compounds, oxides, and organics, the comprehensive performance of Zn@ZSO is at the advanced level (Table S2, Supporting Information). The plating/stripping stability of Zn@Zn–Ti–O electrode was also evaluated (Figure S14, Supporting Information). The corresponding symmetric cell can also run stably for as long as 1600 h with a small voltage hysteresis of ≈ 25 mV.

The excellent long-term cycling stability is a strong proof that the ZSO layer can inhibit the growth of Zn dendrites. Herein, the Zn plating behavior was also explored to further reveal the effect of ZSO layer. The surface of the initial Zn foil is smooth, but the products after plating for 5 min show different and uneven morphologies, mainly including dendrites and flakes (Figure 3c). When plating for 40 min, dendrites and flakes become denser, and they can easily bind the glass fibers (Figure 3d). These products were obtained by ultrasound treatment, and were further analyzed by electron microscopy characterizations. It is found that the flakes are composed of Zn, S, and O elements (Figure S15a, Supporting Information), and the diffraction rings in the SAED pattern (Figure S15b, Supporting Information) can be well-indexed as the $(\bar{1}\bar{2}0)$, $(\bar{1}07)$, $(3\bar{1}2)$, and $(\bar{4}06)$ crystal planes of $\text{Zn}_4\text{SO}_4(\text{OH})_6 \cdot 4\text{H}_2\text{O}$ (JCPDS No. 44-0673). While the dendrites only include Zn

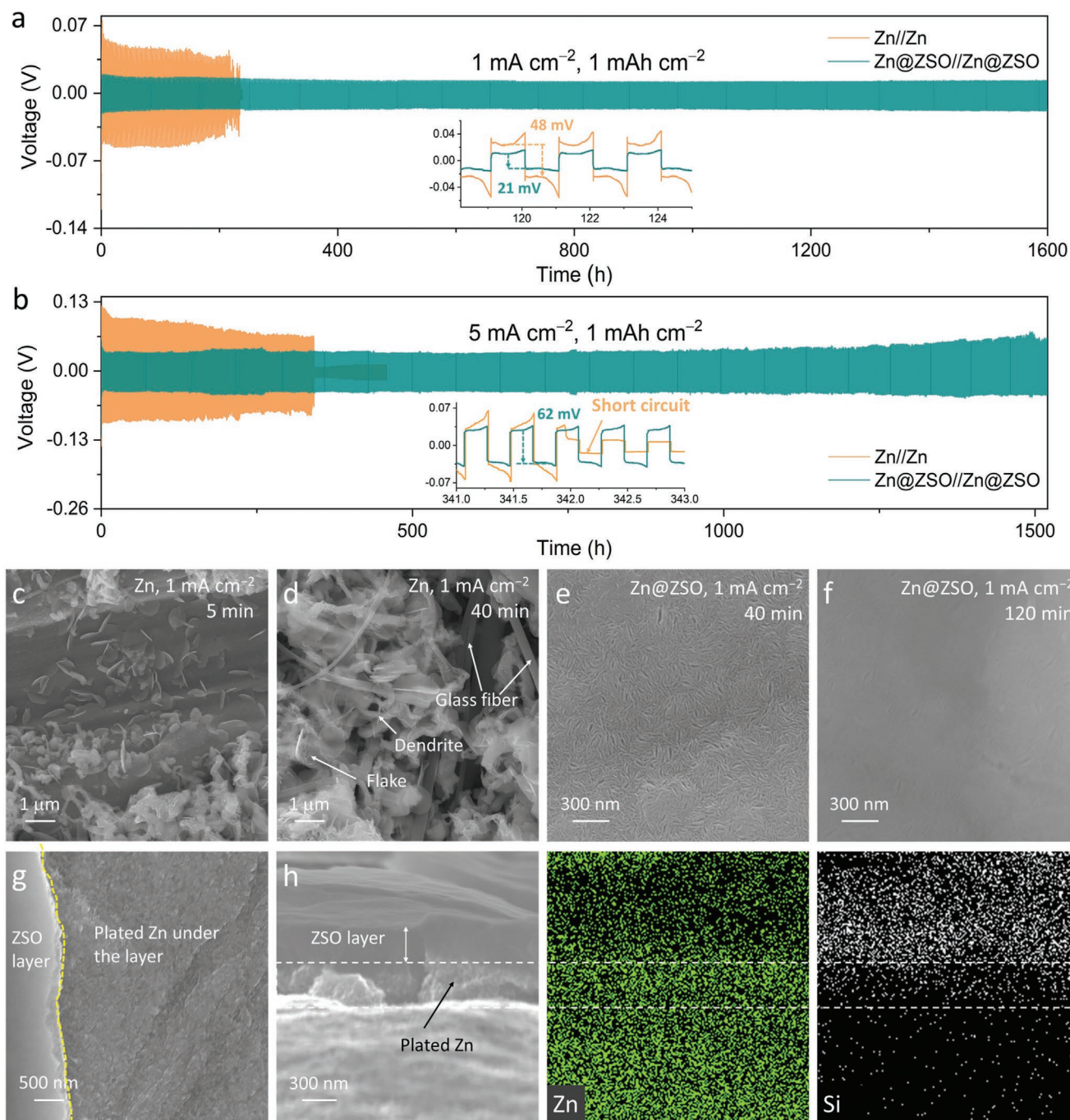


Figure 3. a,b) Galvanostatic cycling performance of Zn//Zn and Zn@ZSO//Zn@ZSO symmetric cells at 1 mA cm⁻² (a) and 5 mA cm⁻² (b) with an areal capacity of 1 mAh cm⁻² (insets: partial Zn plating and stripping curves). c,d) SEM images of Zn plating on Zn electrode for 5 min (c) and 40 min (d). e–g) SEM images of Zn plating on Zn@ZSO electrode for 40 min (e) and 120 min (f,g). h) Cross-sectional SEM image and the corresponding elemental mappings of Zn plating on Zn@ZSO electrode for 2 h. The current density for all the Zn plating experiments was fixed as 1 mA cm⁻².

element and are confirmed as monocrystalline Zn(100) (Figure S15c,d, Supporting Information), which is a direct evidence that Zn tends to plate along the (100) plane and grow into dendrites. Theoretically, the unsmooth surface atom arrangement of Zn(100) can lead to uneven interfacial charge density distribution, so it is prone for dendrite growth.^[36] The low-magnification SEM images of Zn foil after plating for 5 and

40 min (Figure S16a,b, Supporting Information) indicate that Zn plates dispersedly on the surface, and subsequently aggregates at the sites prone to nucleation.

As for Zn plating on Zn@ZSO electrode, its surface does not change visibly after 40 min (Figure 3e). When the areal capacity of Zn plating reaches 1 mAh cm⁻², the surface is clean and smooth on a large scale (Figure S16c, Supporting Information).

As the process continues, the edges of ZSO nanosheets become blurred (Figure 3f and Figure S16d (Supporting Information)). In addition, the small sized, tightly packed, smooth, and uniform Zn is observed below the ZSO layer (Figure 3g). Cross-sectional SEM image and the corresponding element mappings (Figure 3h) show that the plated Zn is closely connected to the bottom of ZSO layer. In addition, digital photos of electrodes after 5, 10, 50, and 100 cycles at 5 mA cm^{-2} and 1 mAh cm^{-2} are shown in Figure S17 (Supporting Information). The surfaces of Zn@ZSO electrodes present a uniform gray color of plated Zn, but which of pure Zn anodes become rougher with dendrites in most of the area when the cycle number is increased. These results indicate that ZSO layer has successfully regulated Zn plating behaviors and inhibited dendrite formation.

2.4. Internal Driving Force of ZSO Layer to Regulate Zn Plating Behavior

Two important questions are to be uncovered in this part, including why Zn plates in a bottom-up order and why it can plate uniformly and smoothly. For the former, the electron/ion transport of the interface layer plays a decisive role.^[22,37,38] The calculated bandgap of ZnSiO₃ is $\approx 3.5 \text{ eV}$ (Figure 4a), and the resistivity of the layer is determined as $9.18 \times 10^5 \Omega \text{ cm}$ (Figure S18, Supporting Information), indicating that it is almost an electronic insulator. In terms of ion transport, the narrow cracks between ZSO nanosheets and the abundant micro-/mesopores on the nanosheets may induce strong capillary forces, which can mightily adsorb the electrolyte

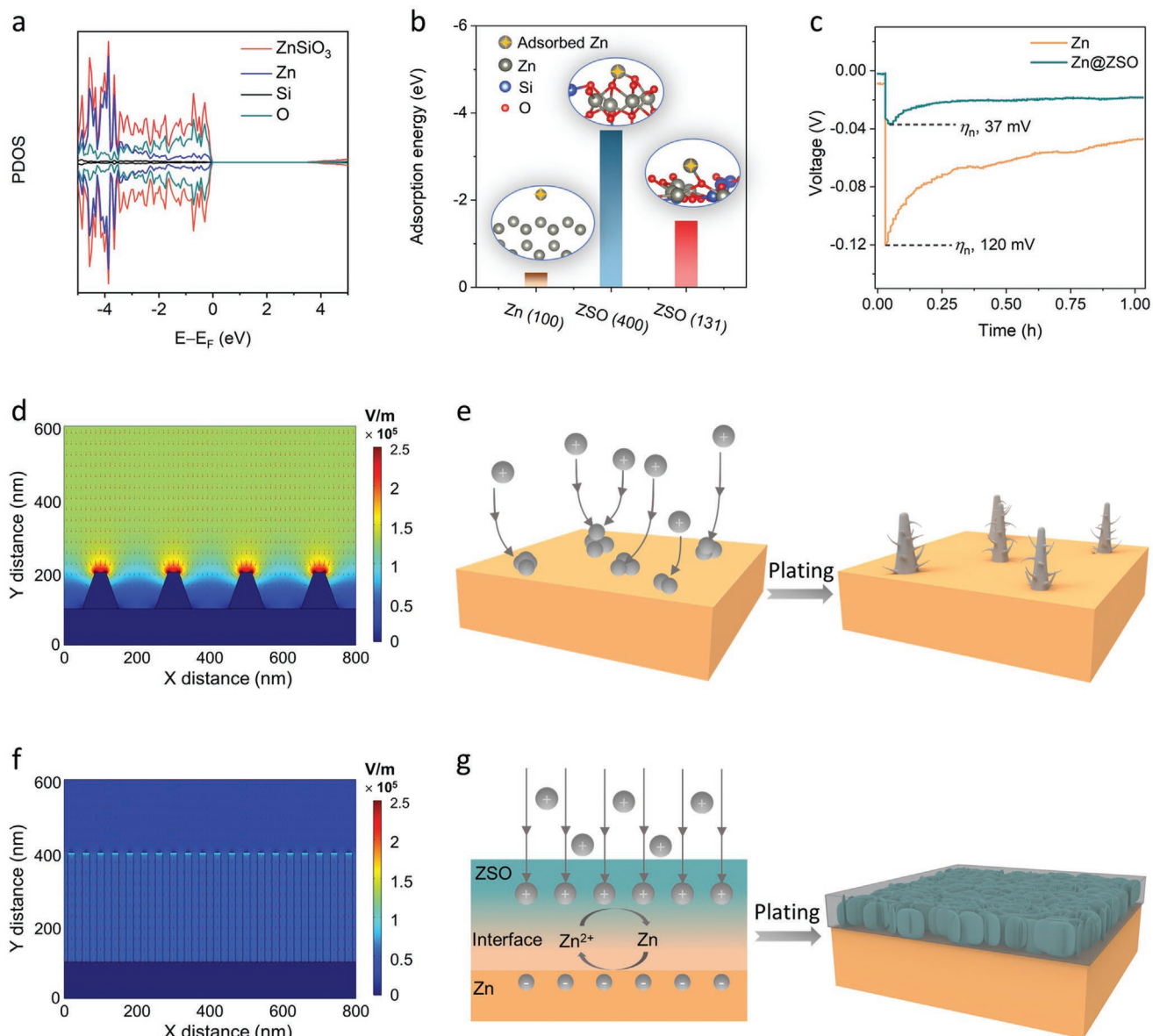


Figure 4. a) Partial density of states (PDOS) of ZnSiO₃. b) Adsorption energies of Zn atom on Zn(100), ZSO(400), and ZSO(131). The insets are the corresponding models. c) Initial discharge voltage–time profiles of Zn plating on bare Zn and Zn@ZSO electrode. d, f) Simulations of electric field distribution of bare Zn with nanosized humps (d) and Zn@ZSO (f). e, g) Diagrams of Zn plating on a Zn anode (e) and a Zn@ZSO anode (g).

and thereby act as the tunnels for Zn^{2+} diffusion. As shown in Figure S19a (Supporting Information), the contact angle of 2 M ZnSO_4 solution on Zn@ZSO surface is 66.8° , much smaller than that of pure Zn (97.6°), confirming the better surface wettability improved by the capillary action. In addition, according to the models calculated by the density functional theory (Figure 4b), the Zn atoms tend to be adsorbed at the oxygen-containing sites in ZnSiO_3 . The calculated adsorption energy of Zn atom on $\text{ZSO}(400)$ (-3.603 eV) and $\text{ZSO}(131)$ (-1.526 eV) is much more negative than that on $\text{Zn}(100)$ (-0.335 eV), confirming the strong zincophilicity of the ZSO layer, which also helps to achieve uniform Zn^{2+} flux. Therefore, the reduction reaction of Zn^{2+} can take place at the interface between Zn foil and the ZSO layer.

In the long-term cycling of Zn plating/stripping in Figure 3a, the Zn@ZSO//Zn@ZSO symmetric cell displays a lower polarization, suggesting the faster Zn plating kinetics. To further demonstrate the effects of ZSO layer on reaction kinetics, the nucleation and growth behaviors of Zn were studied. In voltage–time curve of Zn plating, the initial peak voltage represents the nucleation overpotential (η_n).^[39,40] At 1 mA cm^{-2} , the Zn@ZSO electrode shows an ultralow η_n of 37 mV, much smaller than that of pure Zn (120 mV), as shown in Figure 4c. This implies that the ZSO layer has greatly reduced the energy barrier of Zn nucleation, which could be attributed to the enhanced adsorption of Zn^{2+} by the rich oxygen-containing groups in the layer.^[4,23] As Zn plates continuously, the overpotential gradually decreases as the Zn nucleation becomes easier. It is noteworthy that the overpotential of Zn@ZSO//Zn@ZSO symmetric cell reaches a balanced and stable value (19 mV) at the 18th min, while that of pure Zn is in a continuous decreasing process (47 mV at the end of plating). In theory, a lower overpotential originates from faster charge/mass-transfer processes.^[40] As confirmed by electrochemical impedance spectroscopy (EIS) results (Figure S19b, Supporting Information), the charge transfer impedance (R_{ct}) value of Zn@ZSO//Zn@ZSO symmetric cell (37 Ω) is smaller than that of Zn//Zn symmetric cell (77 Ω), indicating its faster charge transfer process. Besides, the diffusion–nucleation process of Zn^{2+} under a constant voltage was also researched (Figure S20, Supporting Information). When -150 mV voltage bias was applied to the symmetric cell, Zn^{2+} diffuses from the electrolyte toward the surface sites favorable for nucleation through a 2D pathway, which leads to the increased current density.^[31,36,41] After 20 s, the current density of Zn@ZSO//Zn@ZSO remains stable, indicating that the diffusion–nucleation process reached equilibrium, that is, Zn^{2+} could be in situ reduced to Zn at the adsorption sites.^[42] Conversely, the current density of Zn//Zn symmetric cell increases continuously, which is caused by the diffusion and accumulation of Zn^{2+} at the surface of Zn anode. Therefore, the overpotential of Zn@ZSO in Figure 4c that rapidly reaches equilibrium can be attributed to the optimized diffusion–nucleation process. In addition, the fine hydrophilicity and abundant pore structure can also facilitate Zn^{2+} migration and diffusion,^[43] thus accelerating the electrochemical kinetics and reducing the polarization.

The uneven electric field distribution is responsible for the continuous dendrite growth. In general, high conductive layer or skeleton-structured layer with high specific surface area

has been supposed to achieve even electric field.^[30,44,45] Here, the COMSOL method was used to simulate the electric field distribution in the interface of electrolyte and anode (Figure S21, Supporting Information). As shown in Figure 4d,e, the nano-sized humps represent the initial nucleation of Zn on bare Zn anode. The electric field tends to accumulate on the tip of these humps, which would further cause more severe dendrite growth. On the contrary, benefitted from its uniform nanosheet array structure, the ZSO layer can equalize the electric field distribution and reduce the local current density, thus eliminating “tip effect” to achieve even Zn plating (Figure 4f,g).

2.5. Full Cell Performance with the Zn@ZSO Anode

The greatly improved long-term cycling life of symmetric cells verifies the effectiveness of ZSO layer in inhibiting Zn dendrites. Herein, the full cells were also assembled to further evaluate the potential of the Zn@ZSO electrode for practical applications. In order to better evaluate the difference between the anodes, a stable cathode material should be selected. Recently, ion-preintercalated MnO_2 has been confirmed with excellent electrochemical energy storage performance.^[46] Here, $\text{K}_{0.27}\text{MnO}_2 \cdot 0.54\text{H}_2\text{O}$ (KMO) nanoparticles were prepared as the cathode material (Figure S22, Supporting Information). The simple preparation and high yield of 2.5 g at one time can also support the requirements for large-scale pouch cell. The electrochemical performance of coin-type cells was first tested. In the cyclic voltammetry (CV) curves at 0.1 mV s^{-1} (Figure 5a), the two pairs of redox peaks correspond to the stepwise conversion of $\text{Mn}^{4+}/\text{Mn}^{3+}$ and $\text{Mn}^{3+}/\text{Mn}^{2+}$.^[47,48] The oxidation peak located at 1.534 V in Zn@ZSO//KMO shifts to the left by 22 mV compared with that in Zn//KMO (1.556 V), indicating a smaller polarization. According to the EIS results (Figure S23a, Supporting Information), the higher slope in the low frequency region and lower R_{ct} indicate faster ion diffusion and charge transfer in Zn@ZSO//KMO cell. For long-term cycling performance test, to reach deep Zn plating/stripping in anode, the KMO electrode was prepared with a high mass loading of 8 mg cm^{-2} and the applied current density was fixed as 308 mA g^{-1} (1C). As shown in Figure 5b, Zn@ZSO//KMO cell can cycle stably for 400 times (446 h), showing a specific capacity of 156.8 mAh g^{-1} (the corresponding capacity is 0.795 mAh) at the 400th cycle, and its capacity retention is 70.6% when compared to the maximum value. The capacity retention of Zn//KMO is lower (63.8%), and its Coulombic efficiency suddenly increases when reaching the 120th cycle. In the charging process of the 123th cycle, the voltage drops from 1.72 to 1.41 V and keeps charging continuously, indicating that the cell undergoes a short circuit (Figure S23b, Supporting Information). In the reported coin-type full cell test, high-mass-loading cathode has been rarely used, and test parameters (active material, electrolyte, current density, etc.) are commonly not unified. Here, cumulative capacity, a parameter that has been used for comparison in symmetric cells, is introduced to assess the performance in this work. It is a comprehensive presentation of mass loading, areal capacity, and cycle number. As shown in Table S3 (Supporting Information), in the statistical range, 75% of the cumulative capacities are less than

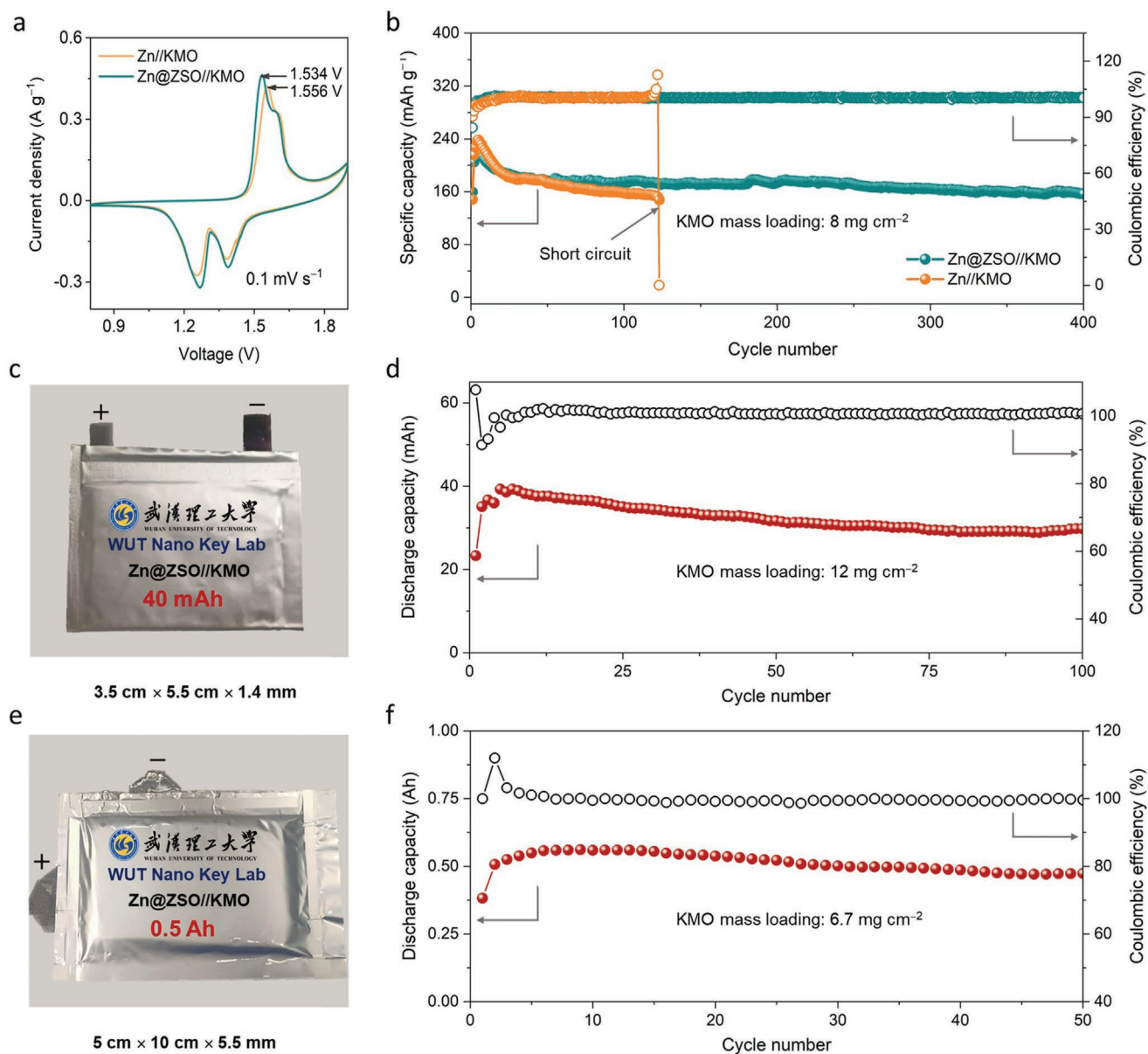


Figure 5. a) CV curves of Zn//KMO and Zn@ZSO//KMO cells at 0.1 mV s^{-1} . b) Long-term cycling performance of Zn//KMO and Zn@ZSO//KMO coin cells. c) Digital photo and d) cycling performance of single-layer Zn@ZSO//KMO pouch cell. e) Digital photo and f) cycling performance of multilayer Zn@ZSO//KMO pouch cell. The voltage window for all cells was tested at 0.8–1.9 V, and the current density was 308 mA g^{-1} .

300 mAh cm^{-2} , and only 12.5% (including this work of $548.9 \text{ mAh cm}^{-2}$) are more than 500 mAh cm^{-2} . In addition, the ratio of the cycling numbers between the modified Zn (experimental group) and bare Zn (control group) is also evaluated for the first time, which is utilized to reflect the effectiveness of the modified layers for Zn anode stabilization. In most reports, the two groups only show a difference in capacity or cycling stability, which is not well consistent with the results of symmetric cells. In this work, the control group shows a failure of short circuit, and the modified Zn@ZSO foil really achieves the purpose of prolonging cell life.

To further evaluate the practicability of the Zn@ZSO anode, the pouch cells were assembled. As mentioned above, the ZSO

layer exists on both sides of Zn foil, so apart from a single-layer pouch cell with size of $3.5 \text{ cm} \times 5.5 \text{ cm} \times 1.4 \text{ mm}$ (Figure 5c), a multilayer (6 cathode + 5 anode) pouch cell with size of $5 \text{ cm} \times 10 \text{ cm} \times 5.5 \text{ mm}$ was also successfully assembled and tested (Figure 5e and Figure S24 (Supporting Information)). They exhibit the open-circuit voltages of 1.443 and 1.407 V, respectively. For single-layer pouch cell, its maximum capacity is 39.3 mAh (Figure 5d), and the areal capacity after 100 cycles is 1.56 mAh cm^{-2} , about 75.7% retention compared with the maximum value (2.06 mAh cm^{-2}). The multilayer pouch cell exhibits a maximum capacity of 561.7 mAh , and a capacity retention of 84.3% after running for 50 cycles at 1C (Figure 5f). When compared with fresh cell, the 0.5 Ah pouch cell after

cycling also shows no significant swelling. Up to now, high-capacity pouch cell in AZIBs has been rarely explored, so the success of high-capacity Zn–MnO₂ pouch cell shows the potential of Zn@ZSO electrode, and provides a referable model.

3. Conclusion

We have developed a low-temperature wet-chemistry strategy with industrial operability to realize the large-scale integration of ZnSiO₃ nanosheet arrays on Zn foil for the first time, and proposed Zn-island-based identical-location scanning electron microscopy characterization to visualize and uncover the in situ integration mechanism of Zn–Si–O layer, which follows the “etching–nucleation–growth” process. The thin ZSO layer shows good stability in 2 M ZnSO₄ solution, which is also insulative, zincophilic, hydrophilic, and porous. Combined with kinetic analysis, theoretical calculation, and COMSOL simulation, the uniform Zn²⁺ flux and fast charge/mass transfer achieved by the ZSO layer facilitate the homogeneous and smooth Zn plating, and finally solve the Zn dendrite issue. As a result, the comprehensive performance of Zn@ZSO anode is at an advanced level. The symmetrical cells run for 1600 and 1520 h at 1 and 5 mA cm⁻² with an areal capacity of 1 mAh cm⁻², about 7.5 and 4.5 times of Zn//Zn symmetric cells, respectively. The full cell with Zn@ZSO anode and high-mass-loading KMO cathode can cycle stably for 400 times at 1C. Furthermore, the large-scale prepared Zn@ZSO facilitates the assembly of a multilayer and large-area pouch cell. The success of 0.5 Ah pouch cell is supposed to provide a referable model for a high-capacity Zn–MnO₂ cell. In short, the low-cost and scalable synthesis method developed in this work, and the smooth Zn plating guided by the structural advantages of the interface layer, are expected to provide a new perspective for the comprehensive design of an interface layer on a Zn anode.

Supporting Information

Supporting Information is available from the Wiley Online Library or from the author.

Acknowledgements

This work was supported by the the National Key Research and Development Program of China (Grant No. 2020YFA0715000), the National Natural Science Foundation of China (Grant Nos. 52127816, 51872218), the Foshan Xianhu Laboratory of the Advanced Energy Science and Technology Guangdong Laboratory (Grant No. XHT2020-003), the Post-Doctoral Innovation Research Project of Hubei Province (Grant No. 20201j003). The S/TEM work was performed at the Nanostructure Research Center (NRC) in Wuhan University of Technology. The authors thank Peijie Wu from the Wuhan University of Technology for the schematic drawing.

Conflict of Interest

The authors declare no conflict of interest.

Data Availability Statement

The data that support the findings of this study are available from the corresponding author upon reasonable request.

Keywords

high-capacity pouch cells, integration mechanisms, large-scale production, uniform Zn plating, zinc metasilicate coatings

Received: March 8, 2022

Revised: April 11, 2022

Published online:

- [1] D. Chao, W. Zhou, F. Xie, C. Ye, H. Li, M. Jaroniec, S.-Z. Qiao, *Sci. Adv.* **2020**, *6*, eaba4098.
- [2] Z. Pan, X. Liu, J. Yang, X. Li, Z. Liu, X. Loh, J. Wang, *Adv. Energy Mater.* **2021**, *11*, 2100608.
- [3] X. Jia, C. Liu, Z. G. Neale, J. Yang, G. Cao, *Chem. Rev.* **2020**, *120*, 7795.
- [4] Z. Yi, G. Chen, F. Hou, L. Wang, J. Liang, *Adv. Energy Mater.* **2021**, *11*, 2003065.
- [5] F. Wang, O. Borodin, T. Gao, X. Fan, W. Sun, F. Han, A. Faraone, J. A. Dura, K. Xu, C. Wang, *Nat. Mater.* **2018**, *17*, 543.
- [6] L. Cao, D. Li, T. Pollard, T. Deng, B. Zhang, C. Yang, L. Chen, J. Vatamanu, E. Hu, M. J. Hourwitz, *Nat. Nanotechnol.* **2021**, *16*, 902.
- [7] B. Tang, L. Shan, S. Liang, J. Zhou, *Energy Environ. Sci.* **2019**, *12*, 3288.
- [8] Q. Yang, Q. Li, Z. Liu, D. Wang, Y. Guo, X. Li, Y. Tang, H. Li, B. Dong, C. Zhi, *Adv. Mater.* **2020**, *32*, 2001854.
- [9] Q. Zhang, J. Luan, Y. Tang, X. Ji, H. Wang, *Angew. Chem., Int. Ed.* **2020**, *59*, 13180.
- [10] L. Yuan, J. Hao, C.-C. Kao, C. Wu, H.-K. Liu, S.-X. Dou, S.-Z. Qiao, *Energy Environ. Sci.* **2021**, *14*, 5669.
- [11] S. Liu, R. Zhang, J. Mao, Y. Zhao, Q. Cai, Z. Guo, *Sci. Adv.* **2022**, *8*, eabn5097.
- [12] D. Han, C. Cui, K. Zhang, Z. Wang, J. Gao, Y. Guo, Z. Zhang, S. Wu, L. Yin, Z. Weng, F. Kang, Q.-H. Yang, *Nat. Sustainability* **2021**, *5*, 205.
- [13] M. Yang, J. Zhu, S. Bi, R. Wang, Z. Niu, *Adv. Mater.* **2022**, *34*, 2201744.
- [14] C. Li, X. Xie, H. Liu, P. Wang, C. Deng, B. Lu, J. Zhou, S. Liang, *Natl. Sci. Rev.* **2022**, *9*, nwab177.
- [15] Z. Liu, Y. Yang, S. Liang, B. Lu, J. Zhou, *Small Struct.* **2021**, *2*, 2100119.
- [16] D. Han, Z. Wang, H. Lu, H. Li, C. Cui, Z. Zhang, R. Sun, C. Geng, Q. Liang, X. Guo, Y. Mo, X. Zhi, F. Kang, Z. Wang, Q.-H. Yang, *Adv. Energy Mater.* **2022**, *12*, 2102982.
- [17] B. Zhang, L. Qin, Y. Fang, Y. Chai, X. Xie, B. Lu, S. Liang, J. Zhou, *Sci. Bull.* **2022**, *67*, 955.
- [18] Z. Zhao, J. Zhao, Z. Hu, J. Li, J. Li, Y. Zhang, C. Wang, G. Cui, *Energy Environ. Sci.* **2019**, *12*, 1938.
- [19] P. Chen, X. Yuan, Y. Xia, Y. Zhang, L. Fu, L. Liu, N. Yu, Q. Huang, B. Wang, X. Hu, *Adv. Sci.* **2021**, *8*, 2100309.
- [20] J. Hao, X. Li, S. Zhang, F. Yang, X. Zeng, S. Zhang, G. Bo, C. Wang, Z. Guo, *Adv. Funct. Mater.* **2020**, *30*, 2001263.
- [21] Q. Zhang, J. Luan, X. Huang, Q. Wang, D. Sun, Y. Tang, X. Ji, H. Wang, *Nat. Commun.* **2020**, *11*, 3961.
- [22] L. Kang, M. Cui, F. Jiang, Y. Gao, H. Luo, J. Liu, W. Liang, C. Zhi, *Adv. Energy Mater.* **2018**, *8*, 1801090.

- [23] P. Liang, J. Yi, X. Liu, K. Wu, Z. Wang, J. Cui, Y. Liu, Y. Wang, Y. Xia, J. Zhang, *Adv. Funct. Mater.* **2020**, *30*, 1908528.
- [24] H. He, H. Tong, X. Song, X. Song, J. Liu, *J. Mater. Chem. A* **2020**, *8*, 7836.
- [25] P. Zou, R. Zhang, L. Yao, J. Qin, K. Kisslinger, H. Zhuang, H. L. Xin, *Adv. Energy Mater.* **2021**, *11*, 2100982.
- [26] M. Liu, J. Cai, H. Ao, Z. Hou, Y. Zhu, Y. Qian, *Adv. Funct. Mater.* **2020**, *30*, 2004885.
- [27] Z. Tu, S. Choudhury, M. J. Zachman, S. Wei, K. Zhang, L. F. Kourkoutis, L. A. Archer, *Joule* **2017**, *1*, 394.
- [28] J. Plutnar, M. Pumera, *Small* **2021**, *17*, 2102088.
- [29] L. Ma, Q. Li, Y. Ying, F. Ma, S. Chen, Y. Li, H. Huang, C. Zhi, *Adv. Mater.* **2021**, *33*, 2007406.
- [30] Y. Yang, C. Liu, Z. Lv, H. Yang, Y. Zhang, M. Ye, L. Chen, J. Zhao, C. C. Li, *Adv. Mater.* **2021**, *33*, 2007388.
- [31] X. Xie, S. Liang, J. Gao, S. Guo, J. Guo, C. Wang, G. Xu, X. Wu, G. Chen, J. Zhou, *Energy Environ. Sci.* **2020**, *13*, 503.
- [32] J. Hao, B. Li, X. Li, X. Zeng, S. Zhang, F. Yang, S. Liu, D. Li, C. Wu, Z. Guo, *Adv. Mater.* **2020**, *32*, 2003021.
- [33] X. Zeng, J. Mao, J. Hao, J. Liu, S. Liu, Z. Wang, Y. Wang, S. Zhang, T. Zheng, J. Liu, *Adv. Mater.* **2021**, *33*, 2007416.
- [34] H. Park, P. Englezos, *Fluid Phase Equilib.* **1998**, *153*, 87.
- [35] K. N. Wood, E. Kazyak, A. F. Chadwick, K.-H. Chen, J.-G. Zhang, K. Thornton, N. P. Dasgupta, *ACS Cent. Sci.* **2016**, *2*, 790.
- [36] M. Zhou, S. Guo, J. Li, X. Luo, Z. Liu, T. Zhang, X. Cao, M. Long, B. Lu, A. Pan, G. Fang, J. Zhou, S. Liang, *Adv. Mater.* **2021**, *33*, 2100187.
- [37] X. Zeng, K. Xie, S. Liu, S. Zhang, J. Hao, J. Liu, W. Pang, J. Liu, P. Rao, Q. Wang, J. Mao, Z. Guo, *Energy Environ. Sci.* **2021**, *14*, 5947.
- [38] C. Deng, X. Xie, J. Han, Y. Tang, J. Gao, C. Liu, X. Shi, J. Zhou, S. Liang, *Adv. Funct. Mater.* **2020**, *30*, 2000599.
- [39] A. Pei, G. Zheng, F. Shi, Y. Li, Y. Cui, *Nano Lett.* **2017**, *17*, 1132.
- [40] P. Biswal, A. Kludze, J. Rodrigues, Y. Deng, T. Moon, S. Stalin, Q. Zhao, J. Yin, L. F. Kourkoutis, L. A. Archer, *Proc. Natl. Acad. Sci. USA* **2021**, *118*, e2012071118.
- [41] J. Ballesteros, P. Díaz-Arista, Y. Meas, R. Ortega, G. Trejo, *Electrochim. Acta* **2007**, *52*, 3686.
- [42] S. Di, X. Nie, G. Ma, W. Yuan, Y. Wang, Y. Liu, S. Shen, N. Zhang, *Energy Storage Mater.* **2021**, *43*, 375.
- [43] R. Yuksel, O. Buyukcakir, W. K. Seong, R. S. Ruoff, *Adv. Energy Mater.* **2020**, *10*, 1904215.
- [44] N. Zhang, S. Huang, Z. Yuan, J. Zhu, Z. Zhao, Z. Niu, *Angew. Chem., Int. Ed.* **2021**, *60*, 2861.
- [45] P. Xue, C. Guo, L. Li, H. Li, D. Luo, L. Tan, Z. Chen, *Adv. Mater.* **2022**, *34*, 2110047.
- [46] Q. Zhao, A. Song, S. Ding, R. Qin, Y. Cui, S. Li, F. Pan, *Adv. Mater.* **2020**, *32*, 2002450.
- [47] Y. Jiao, L. Kang, J. Berry-Gair, K. McColl, J. Li, H. Dong, H. Jiang, R. Wang, F. Cora, D. J. L. Brett, G. He, I. P. Parkin, *J. Mater. Chem. A* **2020**, *8*, 22075.
- [48] L. Liu, Y.-C. Wu, L. Huang, K. Liu, B. Duployer, P. Rozier, P.-L. Taberna, P. Simon, *Adv. Energy Mater.* **2021**, *11*, 2101287.